Accepted Manuscript

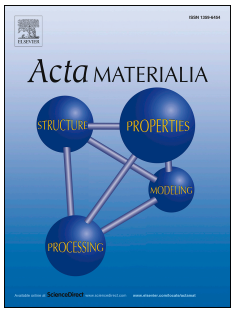

GeV ion irradiation of NiFe and NiCo: Insights from MD simulations and experiments

Aleksi A. Leino, German Samolyuk, Ritesh Sachan, Fredric Granberg, William J. Weber, Hongbin Bei, Jie Lie, Pengfei Zhai, Yanwen Zhang

PII: S1359-6454(18)30256-8

DOI: 10.1016/j.actamat.2018.03.058

Reference: AM 14478

To appear in: *Acta Materialia*

Received Date: 15 November 2017

Revised Date: 21 March 2018

Accepted Date: 22 March 2018

Please cite this article as: A.A. Leino, G. Samolyuk, R. Sachan, F. Granberg, W.J. Weber, H. Bei, J. Lie, P. Zhai, Y. Zhang, GeV ion irradiation of NiFe and NiCo: Insights from MD simulations and experiments, *Acta Materialia* (2018), doi: 10.1016/j.actamat.2018.03.058.

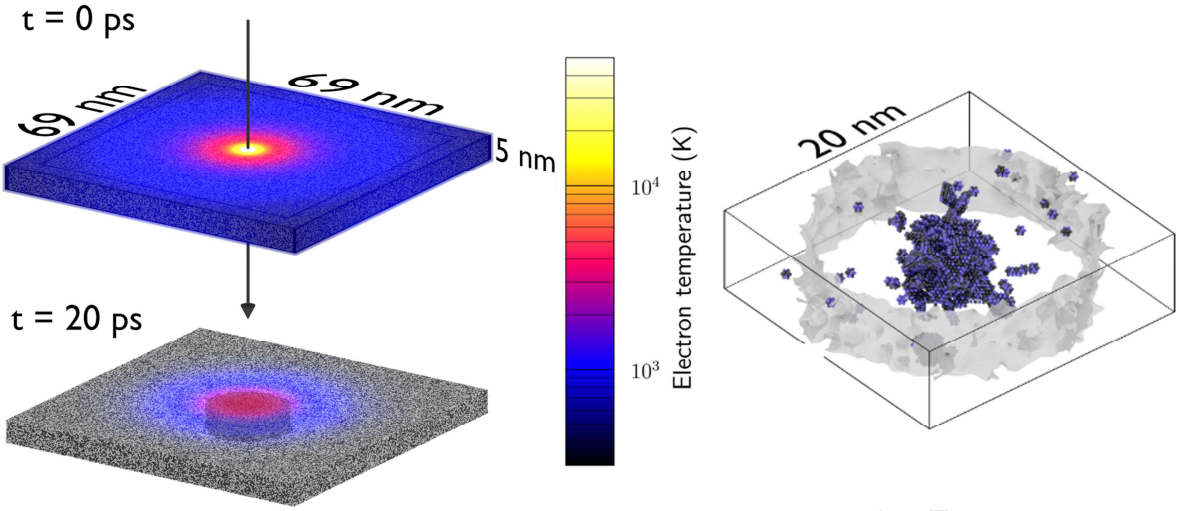

GeV ion irradiation of NiFe and NiCo: insights from MD simulations and experiments

Aleksi A. Leino[1,2], German Samolyuk[1], Ritesh Sachan[1], Fredric Granberg[3], William J. Weber[1,4], Hongbin Bei[1], Jie Lie[5], Pengfei Zhai[5], Yanwen Zhang[1,]*

[1]Materials Science and Technology Division, Oak Ridge National Laboratory, Oak Ridge, TN 37831, USA

[2]Department of Applied Physics, University of Eastern Finland, Post-office box 1627, FIN-70211, Kuopio, Finland

[3]Department of Physics, University of Helsinki, Post-office box 43, FIN-00014, Finland

[4] Department of Materials Science and Engineering, University of Tennessee, Knoxville, TN, 37996, USA

[5] Institute of Modern Physics, Chinese Academy of Sciences, Lanzhou 730000, China

Keywords: nickel alloys; lattice; defects; scanning/transmission electron microscopy (STEM); molecular dynamics

* Corresponding author: zhangy1@ornl.gov, Oak Ridge National Laboratory, Ph: 865-574-8518, Fax: 865-241-3650

Concentrated solid solution alloys have attracted rapidly increasing attention due to their potential for designing materials with high tolerance to radiation damage. To tackle the effects of chemical complexity in defect dynamics and radiation response, we present a computational study on swift heavy ion induced effects in Ni and equiatomic Ni -based alloys ($Ni_{50}Fe_{50}$, $Ni_{50}Co_{50}$) using two-temperature molecular dynamics simulations (2T-MD). The electronic heat conductivity in the two-temperature equations is parameterized from the results of first principles electronic structure calculations. A bismuth ion (1.542 GeV) is selected and single impact simulations performed in each target. We study the heat flow in the electronic subsystem and show that alloying Ni with Co or Fe reduces the heat dissipation from the impact by the electronic subsystem. Simulation results suggest no melting or residual damage in pure Ni while a cylindrical region melts along the ion propagation path in the alloys. In $Ni_{50}Co_{50}$ the damage consists of a dislocation loop structure (d=2nm) and isolated point defects, while in $Ni_{50}Fe_{50}$, a defect cluster (d=4nm) along the ion path is, in addition, formed. The simulation results are supported by atomic-level structural and defect characterizations in bismuth-irradiated Ni and $Ni_{50}Fe_{50}$. The significance of the 2T-MD model is demonstrated by comparing the results to those

obtained with an instantaneous energy deposition model without consideration of e-ph interactions in pure Ni and by showing that it leads to a different qualitative behavior.

1. Introduction

A major challenge in materials science is to understand and predict materials behavior when exposed to ion irradiation. To this end classical molecular dynamics (MD) simulations are often used[1–3]. They provide an atomic-level view of the system under ion study, but do not include a description of the electronic subsystem and are, therefore, limited in applicability to events that involve a low or negligible level of electronic excitations and ionizations.

Several approaches have been developed to address this issue. A prominent method among these is the so-called two-temperature molecular dynamics (2T-MD) model. The model assumes the thermalization and charge neutrality of the electronic subsystem. With these simplifications, the energy dissipation in the electronic subsystem and its coupling to the atomic subsystem can be included without the drastic increase of computational cost that follows from an explicit quantum mechanical description of the excited electronic subsystem.

The term swift heavy ion (SHI) is commonly used to describe ions that are heavier than carbon and with a kinetic energy over 0.5 to 1 MeV per nucleon depending on the atomic mass. SHIs deposit their energy mostly to the electrons along its path before the nuclear stopping takes over at the end of the ion range. Resolving the mechanisms of radiation damage by SHIs is a long-standing challenge in the study of ion-matter interactions[4], and the two-temperature approach depicts one possible path forward. According to the model, in metals, the deposited energy can be expected to dissipate effectively in the electronic subsystem due to high electronic thermal conductivity, and cause only a moderate effect. However, the electronic energy loss is known to cause, for example, an anomalous

annealing of recoil-induced damage in nickel[5] and damaged structures along the ion path in titanium, i.e. ion tracks that are observable by transmission electron microscopy. They seem to consist of dense dislocation loop networks[6]. In the intermetallic compound Ni-Zr_2, amorphous and quasi-continuous tracks have been reported to form[7]. MD simulations of SHI impacts in metals predict the formation of dislocation loops in Fe and W [8].

Recently, Ni-based single-phase concentrated solid solution alloys (CSAs) have gained interest due to their unique physical properties and dramatically enhanced irradiation performance. Among these CSAs, they have been shown to have less damage accumulation than pure Ni when exposed to ion irradiation within the elastic energy loss regime, at least under room temperature irradiation to a low dose[9,10] and elevated temperature to a high dose[10]. As a general trend, the more chemical disorder exists in CSAs, the better radiation resistance is observed. In this Article, to investigate the effect of the alloy composition and chemical disorder in the electronic stopping regime, we have chosen to study Ni, $Ni_{50}Fe_{50}$ and $Ni_{50}Co_{50}$ using 2T-MD simulations. The ion (1.542 GeV Bi) was selected so that its nuclear stopping power (dE/dx_{nucl} = ~ 0.1 keV nm^{-1}) is negligible and the electronic stopping power at its maximum (peak dE/dx_{ele} ranges from 62.28 keV nm^{-1} in $Ni_{50}Fe_{50}$ to 68.85 keV nm^{-1} in Ni), as summarized in Table 1.

In chemically disordered alloys, a stronger effect from the electronic energy loss is expected due to the significantly reduced electron mean free paths (MFPs) compared to pure metals[11]. Therefore, CSAs are ideal systems to test different theoretical approaches to modeling electronic energy loss in metallic targets. It is also noteworthy that the MFPs depend on the alloying elements and concentration, which can be tuned. Moreover, as

pointed out in a recent review[11], CSAs hold distinctive links between tunable scattering processes and energy dissipation, as well as unique correlations between modified energy landscapes and various defect dynamic processes.

Besides importance from a fundamental research perspective, the development and study of the 2T-MD model are relevant for a variety of applications. For example, the model has been shown to have an effect on the residual defect concentration after a recoil simulation at an energy regime relevant for fusion reactor wall materials[12]. We note that the effects of high energy ions are also discussed using the Coulomb explosion[13] and other models in which the interatomic forces are significantly modified[4]. The two-temperature approach and its extensions are under active research also in the laser community[14,15].

2. Methods

2.1. The 2T-MD model

The two-temperature model for radiation damage was introduced in the work of Lifshitz, Kaganov and Tanatarov[16,17]. Separate temperatures are assigned to the atomic and electronic subsystems, noted as $T_a$and T_e, respectively, that evolve according to a heat equation. An additional sink/source term, H, is added to describe the heat absorbed or emitted by the atoms via the electron-phonon coupling. The spatiotemporal evolution of the thermal energy in the electronic subsystem is given by

$$\frac{\partial E_e}{\partial t} = C_e \frac{\partial T_e}{\partial t} = \nabla \cdot (K_e \nabla T_e) + H \quad (1)$$

Here C_e is the electronic heat capacity and $K_e$the electrical heat conductivity. It is useful and conventional to write $H = G(T_a - T_e)$ since, in a high-temperature approximation, H is directly proportional to the temperature difference and G is, therefore, a constant. In

general, G, as well as the rest of the parameters, depend on the electronic and atomic temperature. An often-used practice, which we adopt here, is to consider the electronic temperature dependence of all the parameters only, since the values depend more on T_e than T_a. In the original formulation of the model, accompanied by Eq. (1), there is another heat diffusion equation for the atomic subsystem. Here the 2T-MD model is a compelling alternative and uses molecular dynamics instead. The interaction potential of MD describes e.g. mass transport, pressure waves, superheating and coupling between the optical and acoustic phonon modes[14]. Thereby the number of poorly characterized parameters is substantially reduced.

To connect equation 1 to a MD simulation, the simulation space is divided into small cells, so that equation 1 can be solved on a Cartesian grid. Within each cell, an atomic temperature is calculated from the kinetic energies of atoms. Each cell is assigned an electronic temperature that is evolved by a finite difference (FD) solution of Eq. (1). To represent the energy exchange via e-ph interactions, the MD equation of motion is complemented with a thermostatting term that can add kinetic energy to the atoms or remove it. Several adaptations of the term can be found in the literature (see Supplementary material for more discussion). We use here a simplified version of the one presented in Ref.[18] that has been implemented to the PARCAS simulation code[19,20]. The heat is exchanged in accordance with equation 1 by a damping force in the MD equations of motion[21]

$$F_i = -\nabla V(\{\bar{r}_i\}) + \xi m_i \bar{v}_i$$

The magnitude of ξ is chosen so that the increase in kinetic energy per MD time step corresponds to HV_{cell}, where V_{cell} is the volume of the finite difference grid cell used to

solve equation 1. m_i is the mass of the i:th ion, $\bar{r}_i$ the position and $\bar{v}_i$ the velocity. V is the interatomic potential (in this work, given by Ref. [22]). By taking the derivative of the kinetic energy of the atoms within a cell, it follows that[18]

$$\xi = \frac{V_{cell} G(T_e)(T_e - T_l)}{\sum_i m_i v_i^2}$$

where the sum goes over all atoms in the volume of V_{cell}.

2.2. Model parameters

In 2T-MD simulations, 5 simulation input parameters must be considered: the initial electronic temperature, the electronic heat capacity, the electronic heat conductivity, the effective electron-phonon coupling strength and the force field. Discussion on the initial electronic temperature and the interatomic potential (Zhou, Johnson and Wadley [22]) used is given in the Supplementary material, and the remaining are described in detail in the next subsections.

2.2.1 Electronic heat capacity

The electronic heat capacity was calculated using the standard expression[23]

$$C_e(T_e) = \int_{-\infty}^{\infty} \frac{\partial f(\varepsilon, \mu, T_e)}{\partial T_e} N(\varepsilon) d\varepsilon, (2)$$

where $N(\varepsilon)$ is configurationally averaged electronic density of states (DOS) calculated within coherent potential approximation[24–26]. The chemical potential μ depends from both electron temperature, T_e, and alloy concentration. It is calculated from the constraint to the number of valence electrons. $f(\varepsilon, \mu, T_e) = \{\exp[(\varepsilon - \mu)/k_B T_e] + 1\}^{-1}$ is the Fermi distribution function. Since the most interesting values of the temperature for the current research are above 5000 K, the electronic structures of the alloys were calculated using non-magnetic states. The details and results of CPA calculations can be found in

publication by Samolyuk *et al.*[27] The effect of electronic heat capacity on swift heavy ion track formation has been studied by Khara *et al.*[28]

2.2.3 Effective electron-phonon coupling strength

The calculated electron–phonon coupling strength was obtained using the rigid muffin-tin approximation (RMTA) of Gaspari and Gyorffy[29] and CPA results for electronic structure (see details in the Ref.[27]). In a previous work[30], a reasonable agreement between the time dependent DFT and current approach was obtained for the case of FCC Ni. The electron temperature dependence in the coupling value, $g(T_e)$, was calculated in the spirit of method proposed by Wang *et al.*[31]

$$g(T_e) = \pi\hbar k_B \frac{\eta}{M} N(\varepsilon_F) \int_{-\infty}^{\infty} d\varepsilon \left[\frac{N(\varepsilon)}{N(\varepsilon_F)}\right]^2 \left[-\frac{\partial f(\varepsilon, \mu, T_e)}{\partial T_e}\right], (3)$$

where η is so called Hopfield parameter, M is average mass of the alloy. Hopfield parameter, η, is proportional to electron-phonon coupling constant, $\lambda = \eta/M\langle\omega^2\rangle$, from McMillan expression for superconducting transition temperature[32], where $\langle\omega^2\rangle$ is averaged square of phonon frequency. The formulation with Hopfield parameters instead of λ allows to avoid calculation of phonon frequencies. At the zero temperature, the derivative of Fermi distribution function is reduced to the delta function, $\delta(\varepsilon - \varepsilon_F)$ and the coupling value to $g(0) = \pi\hbar k_B \frac{\eta}{M} N(\varepsilon_F)$. It's worth mentioning that calculated in Ni value $g(T_e)$ is close to result obtained in publication by Lin and Zhigilei[33] and to the available experiment. In the publication, the authors used the experimental value for $g(0)$.

2.2.4 Electronic thermal resistivity

A series of approximations was used to calculate electronic thermal conductivity. First, we assume independent scattering of electrons on electrons, phonons and alloy component disorder[34]. Therefore, total electronic thermal resistivity, w, is equal to

$$w(T_e) = w_{ee}(T_e) + w_{eph}(T_e) + w_0, (4)$$

where w_0 is residual thermal resistivity due to electron scattering on alloy component disorder. Residual thermal resistivity is measured in the limit of zero Kelvin temperature. The electron-phonon contribution is calculated using lowest-order variational approximation to solve the Boltzmann equation to electron transport[34]. Together with the Debye model approximation to electron-phonon spectral (Eliashberg) function[35] the electronic resistivity is

$$w_{eph}(T_e) = \frac{6\Omega_{cell}}{\pi\hbar k_B N(\varepsilon_F)\langle v_x^2\rangle} 2\lambda_{tr}(T_e)\left(\frac{2T_L}{T_D}\right)^4 \int_0^{T_D/2T_L} \frac{x^5 dx}{\sinh^2 x}, (5)$$

where T_e and T_L (300 K for all alloys) are electron and lattice temperatures respectively, Ω_{cell} is the elementary cell volume, $N(\varepsilon_F)$ corresponds to electronic density of state per Ω_{cell} and per spin, $\langle v_x^2\rangle$ is average square of x-component of Fermi velocity, T_D is Debye temperature (450 K), and $\lambda_{tr}(T_e)$ is the transport electron-phonon coupling constant. As it was demonstrated by Allen[35], the transport λ_{tr} can be approximated by λ without significant loss in accuracy. The temperature dependence of the coupling can be calculated using Eq. (3) and relation between λ and Hopfield parameter, η. Finally, the Debye temperature is kept equal to the one in Ni.

Following Lin and Zhigilei[33] the electron-electron scattering contribution to the electronic thermal conductivity is calculated using Drude model[23], $\kappa_{ee} = \langle v_x^2\rangle C_e \tau_{ee}$, where τ_{ee} is the electron relaxation time, $1/\tau_{ee} = AT_e^2$, where A is constant. The values of

the constants for Ni vary from 1.4×10^6 1/K^{2}s for Ni[33,36] to 5.9×10^6 1/K^{2}s[37] (see discussion in Ref.[38]). Below the same value for A has been used for all Ni based alloys. It should be mentioned that at temperatures below the Fermi temperatures, the electron-phonon scattering gives main contribution. Finally, since $w(T_e) = 1/\kappa$, the Eq. (4) can be applied to calculate total electronic thermal conductivity. The residual thermal resistivity, w_0, is taken from the experimental data[39] at 50 K. The κ at 50 K equal to 328, 48.1 and 11.4 W/K·m for Ni, $Ni_{50}Co_{50}$ and $Ni_{50}Fe_{50}$, respectively. The calculated for the case of Ni $v_x = 0.1 \times 10^6$ m/s^2 was used for all alloys. This approximation was verified for the case of ordered $Ni_{50}Fe_{50}$ and $Ni_{50}Co_{50}$ and it was found that deviation from Ni Fermi velocity is small. $N(\varepsilon_F)$ is equal to 22.3, 16.1 and 13.3 States/(Hartree· Spin) for Ni, $Ni_{50}Co_{50}$ and $Ni_{50}Fe_{50}$, respectively.

It should be noticed that instead of approach proposed in the current publication, the thermal conductivity could be alternatively calculated using Kubo-Greenwood formalism[40,41].

2.3. Molecular dynamics setup and analysis

The simulation cell size was chosen to be (69 nm, 69 nm, 5 nm) and the crystal was oriented having the <001> -axis aligned with the z-direction, the same direction as the ion is intersecting the simulation cell. A schematic picture of the simulation cell is given in figure 1. 169×169×1 finite difference cells were used for the heat equation solver. A time step of 0.08 fs was selected to conserve the total energy in the system. This value is lower than needed for most MD simulations.

Experimentally, the irradiation was performed at room temperature, so that far away from the impact location the temperature (at low fluence rates) reaches 300 K. Motivated by this, Dirichlet boundary conditions (boundary temperature=300 K) were imposed on equation 1 in the four planes that are parallel to the ion path and far away from the ion impact location (see figure 1). Zero-flux/periodic condition (these are identical when there is no gradient in the z-direction) was imposed on the remaining two planes (the planes that the ion path intersects, shown by the text 'periodic' in figure 1). In addition, the atoms were quenched at a rapid rate of 0.3 K / fs towards 300 K in the boundary cooling region (also shown in figure 1) by a Berendsen thermostat. The purpose of the procedure was to dampen the pressure waves and to mimic ionic heat conduction to the bulk. Periodic boundary conditions were imposed on the atom movement at all boundaries.

The electronic boundary can be implemented in other ways, such as using the Robin boundary condition[8]. Some of the methods involve new parameters to the model. Our current choice does not; however, the electronic boundary condition overestimates the heat conduction from the system. We have checked that in nickel (the system where heat dissipates fastest) that using a zero-flux boundary condition (which underestimates the heat conduction) does not have a significant effect on the result. We emphasize that the simulation cell must be sufficiently large in the directions perpendicular to the ion path. The width of the ionic boundary cooling region was 2.5 nm. We also checked that a larger boundary cooling region (width 5 nm) did not change the results considerably (melt radius). More discussion on the finite size effects is given in the Supplementary material.

An alternative way that does not involve new parameters or overestimate the heat conduction was used in Ref. [42] (1D geometry) and Ref. [43] (cylindrical/radial

geometry). In that approach, the solution of equation 1 is extended beyond the borders of the MD simulation cell with an accompanying lattice heat equation. Furthermore, the boundaries transmit pressure. Simulations utilizing those boundary conditions could be done as future work.

The Dislocation Extraction Algorithm (DXA)[44], as implemented in the OVITO[45] software, was used to identify dislocation lines and defective volumes from the final atomic configurations. The evolution of the melt radius during the simulation was determined using a three-stage process. In the first stage, atoms with centrosymmetric parameter[46] less than five are removed. After this stage, some atoms that are part of the solid region are left. These atoms are removed by calculating the Voronoi volumes of the atoms that remain, and selecting those with a volume higher than 14 cubic Ångströms. Finally, a surface is constructed[45] from the remaining atoms. It accurately captures the melt-solid interface in all the targets, as is seen in figure 2.

Radial strain fields were present in some of the final atom configurations, which causes artefacts in Wigner-Seitz defect analysis. Therefore, to quantify the defect concentrations in the systems, we applied Polyhedral Template Matching[47], bond-angle analysis[48] and adaptive Common Neighbor analysis[49]. All the methods give the number of atoms that are not in the FCC configuration.

To reduce the numerical noise, we calculated the density profiles using the Voronoi-volumes. That is, instead of using the volume of concentric cylindrical shells as a divisor, we use the sum of the Voronoi volumes of each atom in the shell. This removes the problem that some shells will have intrinsically less atoms due to the crystal structure and makes the values less dependent on the chosen cylinder shell thickness.

2.4 Scanning Transmission Electron microscopy characterization.

The bright field (BF) imaging was performed using an aberration corrected Nion UltraSTEM operating at 200 KV. The collection semi-angle used for the BF imaging was 0-15 mrad and the probe current was 28±2 pA. To analyze the size and circularity distribution to determine the formation of stacking fault tetrahedra (SFT) and dislocation loops, the background of the obtained images were first normalized, followed by color thresholding on the damage regions. The observed features smaller than 1 nm, while relevant to simulations results of defect clusters, were ignored in the analysis due to high uncertainty and considered as an artifact.

3. Results and discussion

3.1. Electronic parameters

The parameters resulting from the KKR-CPA calculations for the heat diffusion Eq. (1) are shown in figure 3. While the electronic heat capacity is comparable in magnitude for the systems studied here, differences occur in the electron-phonon coupling strength and more so in the electrical heat conductivity. The decrease in electron-phonon coupling is due to the sharp spike in the density of states at the Fermi level in pure Ni, which is less pronounced in the alloys and results in a less steep decrease[27]. Since, according to Eq. (4), $w_{ep} \sim g(T_e)$, larger thermal conductivity corresponds to smaller e-ph coupling. Thus, largest thermal conductivity corresponds to Ni and the smallest one to $Ni_{50}Fe_{50}$. The electron-electron scattering suppresses the thermal conductivity as the temperature approaches 10^5 K.

3.2. Initial energy density

The electronic and nuclear stopping power (see table 1) in the surface region, about 5 microns from the surface, of the 1.542 GeV Bismuth ion are similar in all the targets due to similar target density. Utilizing expressions from delta-ray theory (see Supplementary material) and by an integration of the stopping power, the energy density can be calculated as a function of depth from the surface. The initial energy density does not vary much (see figure 4) during the first 20 microns in all the targets. Therefore, we use the surface energy density distributions, but a similar effect is expected at least throughout the first 20 microns. For consistency, the stopping powers used in the simulations are calculated based on the densities of the MD simulation cell and not on the experimental values. The difference is about 1%.

3.3. Heat flow and temperature evolution

The importance of considering the electronic subsystem becomes evident from figure 5, which shows the total energy transfer during the simulation. It was obtained by integrating the H term in equation 1 over the entire simulation length in post-processing. The figure also shows the evolution of the electronic temperature in nickel. The variations in the energy deposition seen in the graphs are consistent with residual damage observed in the simulations (see section 3.4.). Interestingly, the total energy deposition to the atoms near the ion path and the residual damage follows an opposite trend as the electronic stopping power.

Detailed graphs depicting the magnitude of the different terms in the heat equations are given in the Supplementary material. During the initial stages of the simulation ($t < 500$ fs), the differences in the rate of energy deposition from the electrons to the ions are not very pronounced, but can be observed near the ion intersection point (r=0). It is worth noting

that while $Ni_{50}Fe_{50}$ has a higher effective electron-phonon coupling, $Ni_{50}Co_{50}$ has higher stopping power (dE/dx_{ele} = 65.9 keV nm^{-1}) than $Ni_{50}Fe_{50}$ (dE/dx_{ele} = 63.1 keV nm^{-1}) and similar comparison holds for $Ni_{50}Co_{50}$ and Ni. This evens out some of the difference in the energy deposition initially. Significant differences can be seen in the initial rates of diffusion, i.e. in the energy dissipation by the electronic subsystem. The energy dissipation by the electronic subsystem is reduced in $Ni_{50}Fe_{50}$ compared to $Ni_{50}Co_{50}$, while the dissipation is fastest in Ni. By 5 ps, differences also in the energy deposition are evident.

Because of the electronic heat conduction, the temperature of the electronic subsystem reaches the temperature of the lattice fastest near the intersection point of the ion, resulting in cooling of the ions by the electrons. This process is fastest in Ni. By ten picoseconds, almost the entire ionic subsystem in the Ni simulation cell is cooled down by the electrons, whereas $Ni_{50}Co_{50}$ and $Ni_{50}Fe_{50}$ are only partially cooling (the rest is heating). A larger volume is still being heated in $Ni_{50}Fe_{50}$ than in $Ni_{50}Co_{50}$.

3.4. Damage production

A pressure wave develops in the middle of the simulation cell that travels towards the cell boundaries. Four distinct pressure fronts can be observed that travel in the <110> directions. Visualization of the pressure wave is given in the supplementary material. The amplitude is the highest in $Ni_{50}Fe_{50}$ and decreases in magnitude in $Ni_{50}Co_{50}$ and Ni. A cylindrical, molten channel is formed along the ion path in the alloys. Shown in figure 6 are the resulting radii of the channel. While the initial radii are similar in magnitude (r=9 nm), substantial differences exist in in the lifetimes of the molten channels (60 ps in $Ni_{50}Co_{50}$ and 120 ps in $Ni_{50}Fe_{50}$). This is consistent with the heat flow (see section 3.3) in the electronic subsystem – the energy deposition is almost identical initially, but soon becomes

smaller in $Ni_{50}Co_{50}$. The recrystallization rate follows the same trend as electronic heat conductivity; the radius of the molten track decreases at the rate of 0.18 nm/ps in $Ni_{50}Co_{50}$ and 0.11 nm/ps in $Ni_{50}Fe_{50}$.

After 200 ps, to remove thermal noise from the samples, the simulations were relaxed to 0 K and 0 GPa in a 5 ps run before further analysis. The dislocation lines, extracted by the DXA algorithm, are shown in figure 7. In $Ni_{50}Co_{50}$ a single dislocation loop structure forms. In $Ni_{50}Fe_{50}$, a defective volume, accompanied by dislocation lines, is formed. It intersects the simulation cell along the ion beam direction. However, a limitation of the current computational approach is the small simulation cell in the z-direction to keep the calculations feasible. It is unclear if such defect structures will be continuous with a larger cell. In all the samples, the vacancies are scattered in the recrystallized region whereas interstitials tend to agglomerate, as observed in previous simulations in other metallic targets[8,50]. We have also analyzed the simulation cells for local compositional changes by divining the simulation cells into concentric cylinder shells (centered at the ion impact location) of equal atom count (5000). No local compositional changes could be observed. Most of the damage is confined within the molten region.

Experimentally, the ion tracks can be analyzed using small angle x-ray scattering measurements. This technique is sensitive to the density changes due to latent tracks and can be used to deduce its average size with a spatial resolution of few Ångströms. A radial density profile obtained from MD simulations can be used to interpret the scattering pattern[51,52]. Shown in figure 8 are the radial density profiles that were extracted from the cells, which may guide experimental design for validation. An under dense region is seen in $Ni_{50}Fe_{50}$, however, the maximal relative change in density is only about 1%.

The 2T-MD results are validated experimentally by comparing the microstructure modification from SHI irradiations in Ni and $Ni_{50}Fe_{50}$ performed using the annular bright field imaging in a scanning transmission electron microscope (STEM). High quality Ni and $Ni_{50}Fe_{50}$ single crystals were irradiated with 1.542 GeV Bi ions to a fluence of 2×10^{12} ions cm^{-2}. The density of Ni and $Ni_{50}Fe_{50}$ is 8.908 g cm^{-3} (9.14×10^{22} atoms cm^{-3}) and 8.2326 g cm^{-3} (8.66×10^{22} atoms cm^{-3}), respectively. The STEM samples are taken 5 µm from the surface. At this depth in ion energy reduces to 1.20 and 1.23GeV where electronic stopping power dE/dx_{ele} is 68.8 and 62.8 keV nm^{-1} and nuclear stopping powers dE/dx_{nucl} is 0.128 and 0.113 keV nm^{-1} in Ni and $Ni_{50}Fe_{50}$, respectively. The extreme inelastic interactions of ions with target electrons and subsequent heat dissipation to lattice produce structural defects that are observed to be darker than the matrix due to strain diffraction contrast, as shown in Figure 9 (for Ni (a, c) and $Ni_{50}Fe_{50}$ (b, d) respectively. While less damage is identified in Ni than that in $Ni_{50}Fe_{50}$ (Figure 9(b)), both interstitial-type dislocation loops and vacancy-type SFT (Figure 9(a)) are observed in both materials. Since ion-solid interactions are stochastic processes, some ion strikes may cause more damage than others. Comparison between the STEM characterizations with the simulation results should be qualitative. Nevertheless, more damage (SFT and dislocation loops) is evident in $Ni_{50}Fe_{50}$ and can be attributed to the significantly modified MFPs. The much shorter MFPs in $Ni_{50}Fe_{50}$[11,39] lead to slower heat dissipation along the ion path. The extreme localized hot zone along the ion path coupled with the rougher energy landscapes in concentrated alloys result in defect formation[53]. On the other hand, longer MFPs in Ni lead to rapid energy dissipation and less damage formation upon electronic energy deposition from GeV ions, as is expected. Based on the circularity, the damage structures are identified as SFT

(circularity 0.3-1.0) and as dislocation loops (0-0.3). The relative concentration of SFT and dislocation loops are shown in Figure 9c and 9d as the insets respectively for Ni and $Ni_{50}Fe_{50}$ overlaid with background normalized image used for the feature analysis. The modified region in $Ni_{50}Fe_{50}$ has a similar dimension as predicted in figure 7 for $Ni_{50}Fe_{50}$.

In the simulations, no residual damage is produced in pure Ni but much damage is determined in $Ni_{50}Fe_{50}$ (figure 10 shows the residual defect concentrations), qualitatively consistent with the experimental trends shown in figure 9a and 9b. It should be noted that previous continuum calculations using the two-temperature model suggest that damage is formed in Ni, which was considered to be a discrepancy[54] with the available experimental data. This demonstrates the importance of the accurate parameterization and the atom-level description provided by the 2T-MD technique to study radiation damage from a swift heavy ion. It also underlines the importance of the electronic subsystem in the 2T-MD technique, as the simpler energy deposition schemes in regular MD do not lead to the same behavior, as is demonstrated below.

3.5. Comparison between the 2T-MD and the ion energy deposition model

The simplest method to simulate SHI is to omit the details of the energy transfer mechanism, and simply deposit energy to the ions as kinetic energy. This is physically feasible if the timescale on which the energy transfer occurs is very short. To study the significance of the energy deposition model, we run a simulation of an impact in nickel so that the energy density predicted by the equation discussed in the Supplementary material is used to instantaneously add kinetic energy to the atoms while the system evolves without the friction term in the MD equations of motion. Figures 6, 7 and 8 also show results from the instantaneous energy deposition scheme. In this simulation, a molten track with a

lifetime of 170 ps forms. The recrystallization rate is 0.06 nm/ps and a high density of dislocation lines that extend through the periodic simulation cell form. Furthermore, defects form also outside of the region that melted. The sudden expansion of the lattice causes stacking fault planes that aligned along the ion beam direction to form outside of the molten zone. They eventually disappear, but leave behind a trail of defects. This in contrast to the 2T-MD energy deposition model, where the damage is contained within the molten region. The residual defect concentration is two orders of magnitude higher with the instantaneous energy deposition model than with 2T-MD simulations in $Ni_{50}Fe_{50}$. Both comparisons between the 2T-MD and the instantaneous energy deposition model and between the 2T-MD and experimental observation further demonstrate the importance of considering electronic effects and the importance of correctly modeling the electronic subsystem in materials response to extreme ionization irradiation.

4. Conclusions

We modeled the effects of a 1.542 GeV Bi ion impacts in Ni, $Ni_{50}Co_{50}$, and $Ni_{50}Fe_{50}$ using 2T-MD simulation model with a parametrization directly calculated from first principles. The simulation results show that high concentration alloying leads to a reduced energy dissipation by the electronic subsystem. A region melts along the ion path in the alloys while no melting or detectable damage production in pure Ni was obtained. In contrast, using the instantaneous energy deposition model with classical MD, a molten track forms and significant damage production is obtained. Compared to $Ni_{50}Co_{50}$ (60 ps), the lifetime of the molten track has a two-fold increase in $Ni_{50}Fe_{50}$ (120 ps) in 2T-MD. A dislocation loop structure and isolated point defects form in both alloys. In $Ni_{50}Fe_{50}$, a defect cluster forms along the ion path while this did not appear in $Ni_{50}Co_{50}$. Therefore, the

residual defect concentration induced by a single ion impact in $Ni_{50}Fe_{50}$ is notably higher (20 x) than in $Ni_{50}Co_{50}$. The simulations results were compared with STEM characterizations of irradiated samples with identical ion. Experimental atomic-level defect characterizations of NiFe and Ni support the 2T-MD results in the sense that more damage is observed in NiFe. These results suggest that the 2T-MD model, when provided with an accurate parametrization, can be used model the energy dissipation after a swift heavy ion impact in concentrated solid solution alloys. Furthermore, the results suggest that Ni-based alloys have remarkable differences in their responses to electronic energy loss depending on the composition. This insight should be taken into consideration in the design of radiation tolerant concentrated solid solution alloys.

Acknowledgments

This work was supported by Energy Dissipation to Defect Evolution (EDDE), an Energy Frontier Research Center funded by the U.S. Department of Energy, Office of Science, Basic Energy Sciences. The simulation used resources of the National Energy Research Scientific Computing Center, supported by the Office of Science, US Department of Energy, under Contract No. DEAC02-05CH11231. AL acknowledges the support of Jane and Aatos Erkko foundation in Finland for his time on revising the manuscript.

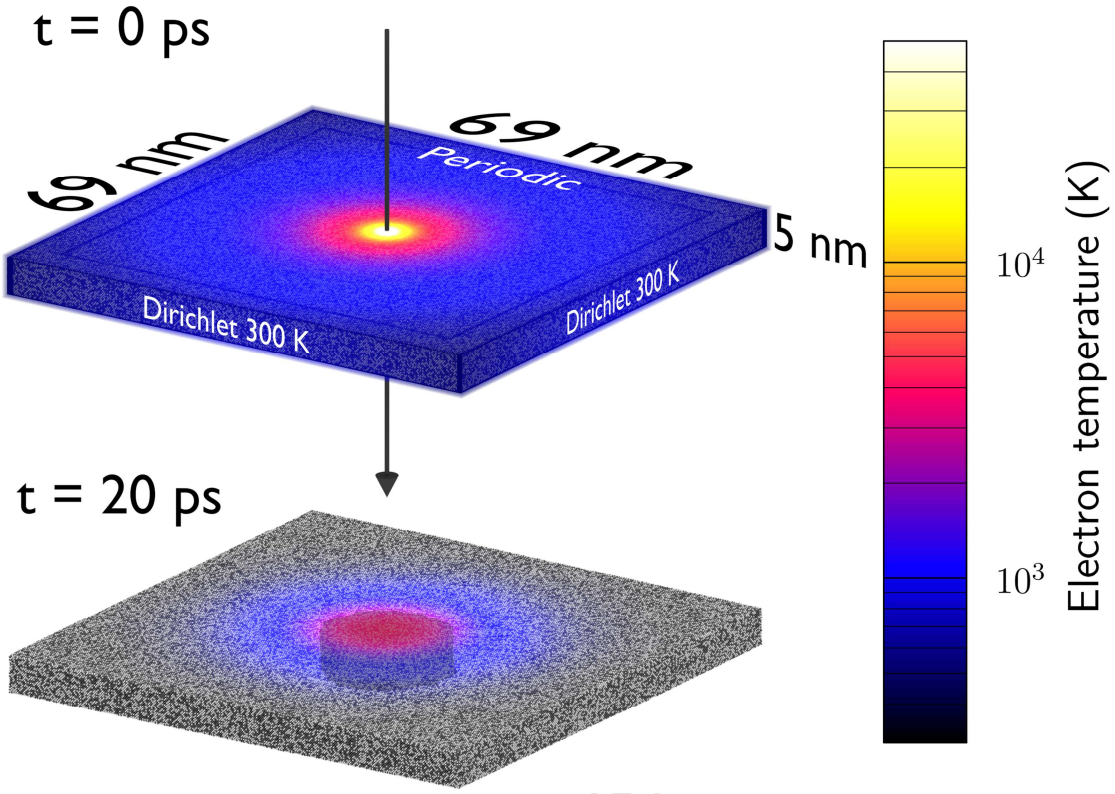

Figure 1. Simulation cell schematics. Schematic picture of the simulation setup ($Ni_{50}Fe_{50}$ simulation cell). Shown by the dark lines in the upper figure is the boundary cooling region for ions. All ion borders are periodic. The white text in the upper figure indicates the electronic boundary conditions for the six planes in the simulation cell. The lower figure shows the simulation cell at a later instance. Color online only.

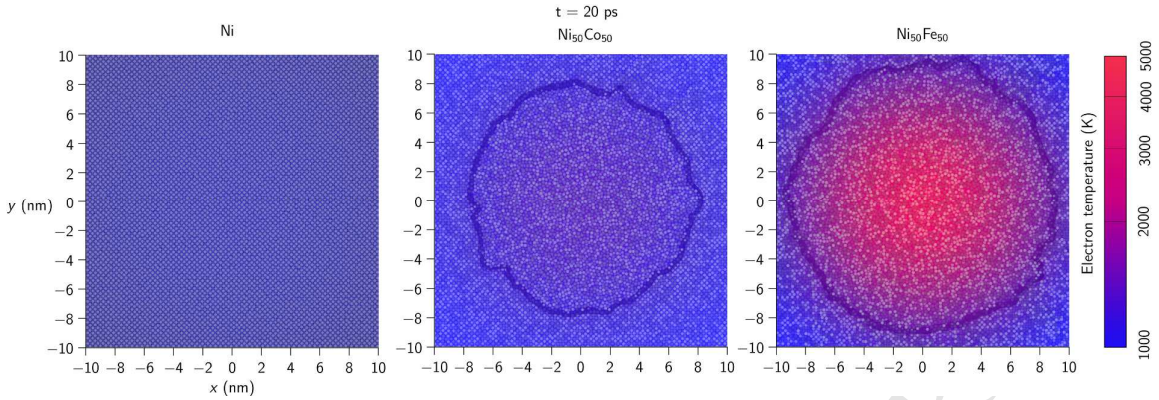

Figure 2. Electronic temperature. Snapshot of the MD simulation cells 20 ps after the impact. Shown by the dark line is the solid-melt interface and by color the electron temperatures. No melting or residual damage is observed in pure Ni. color-web only, 2-col.

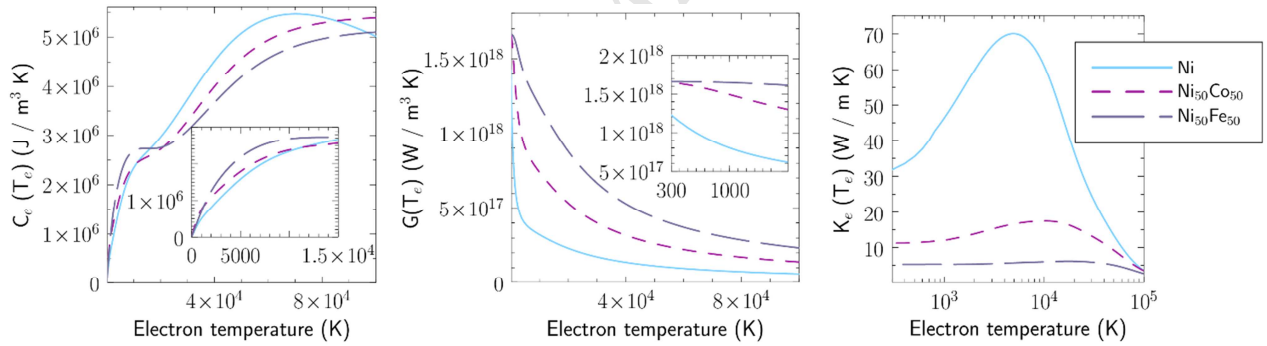

Figure 3. Model parameters. The electronic specific heat capacity, effective electron-phonon coupling strength and electronic heat conductivity for Ni, $Ni_{50}Co_{50}$ and $Ni_{50}Fe_{50}$. Color online only.

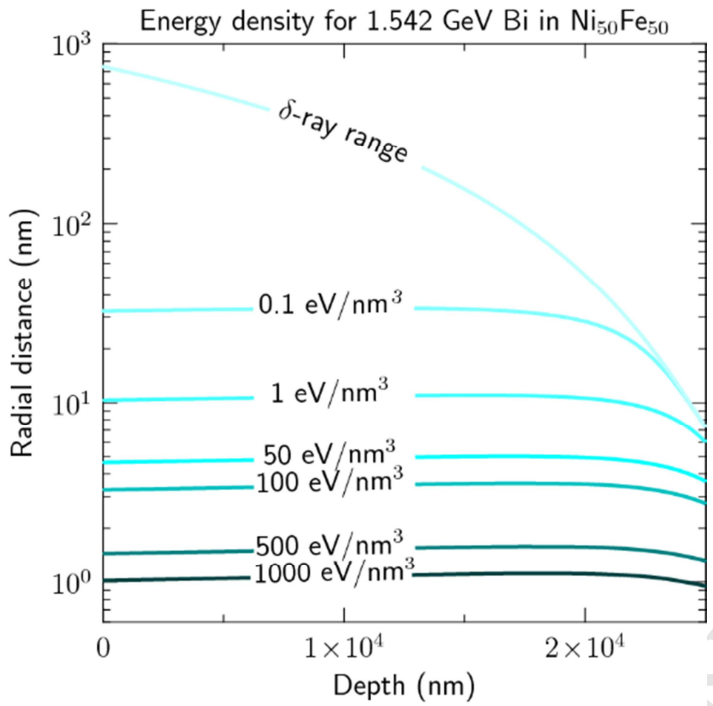

Figure 4. Dose as a function of depth. Dose as a function of radial distance to the ion path and depth from the sample surface assuming a straight path. Shown is the result for $Ni_{50}Fe_{50}$, but the diagram is similar for all investigated targets. Color online only.

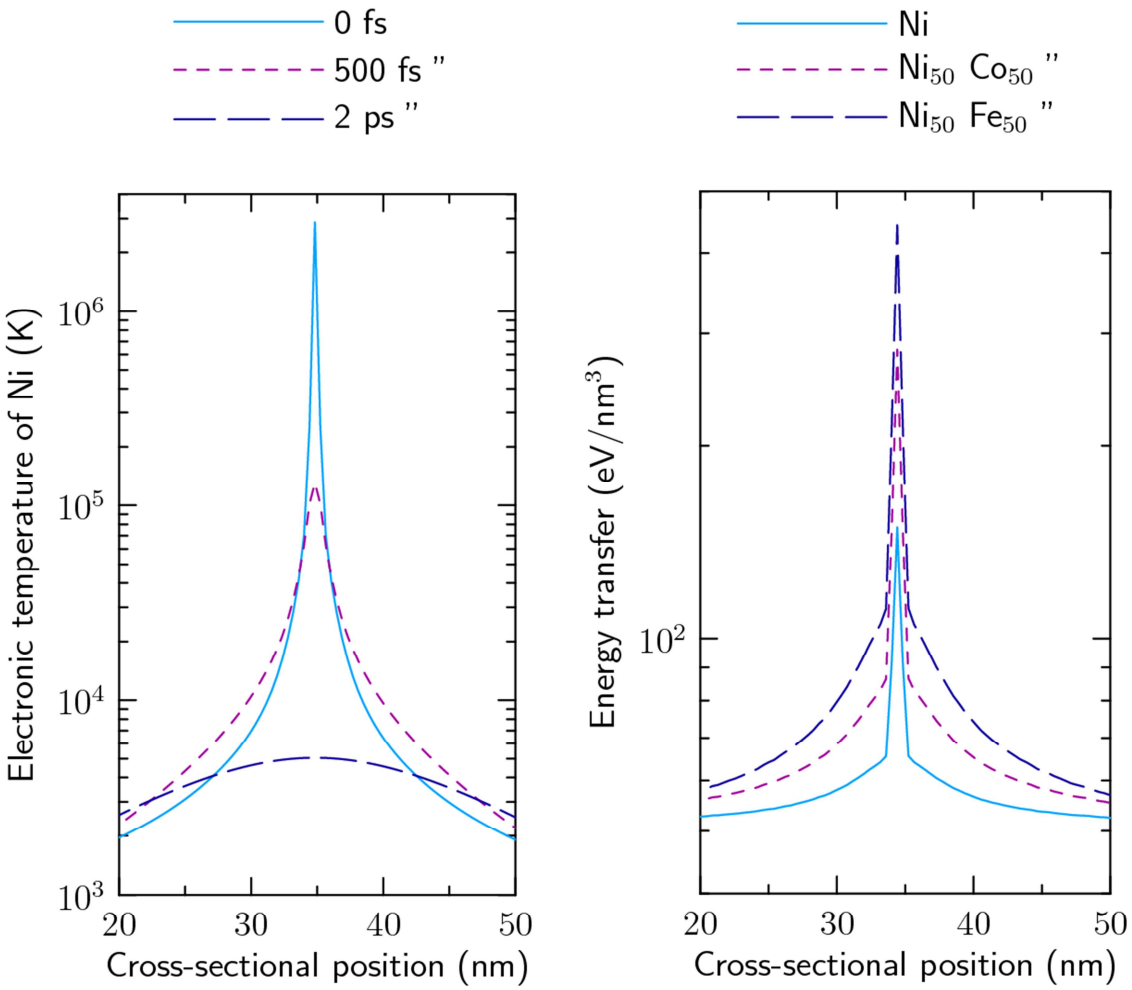

Figure 5. Electronic temperature and total dose. Left: Evolution of the electronic temperature in Ni. Right: Total energy transfer from electrons to the lattice. The values were calculated by integrating H in Eq. (1) over the entire simulation, 200 ps in post-processing. Color online only.

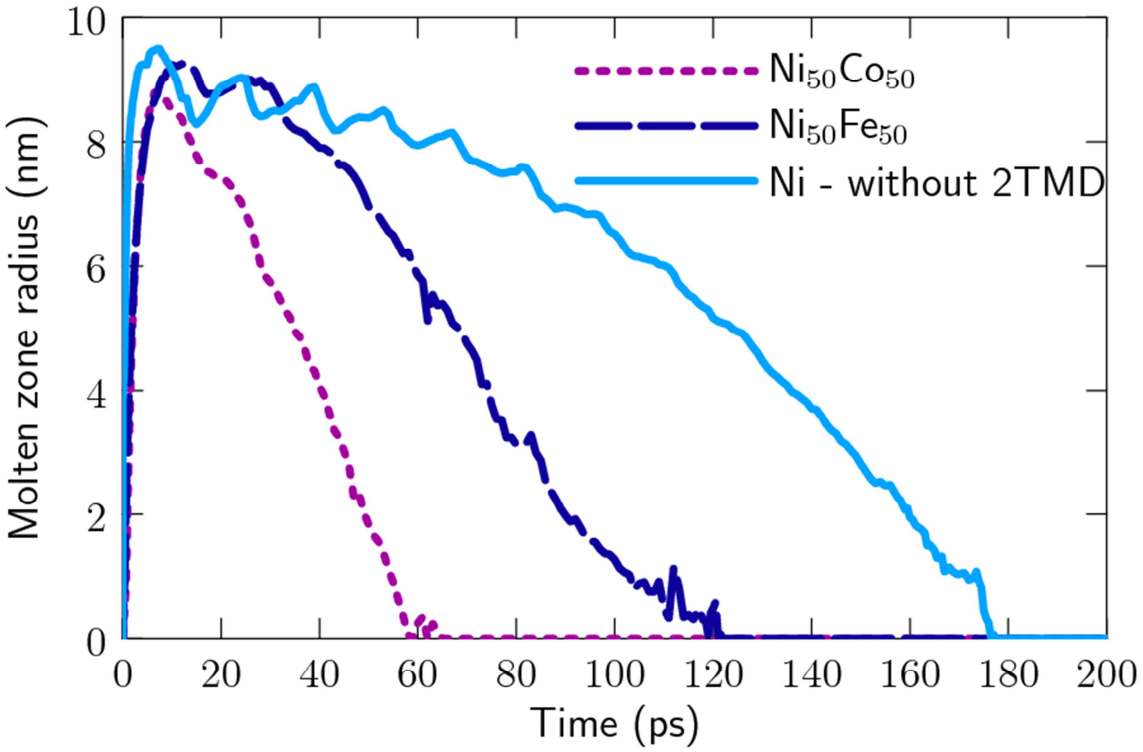

Figure 6. Molten track radius. Estimate of the molten track radius as function of time (top). No molten track forms in Ni in the 2T-MD simulation. Shown is the result using instantaneous energy deposition scheme." Color online only.

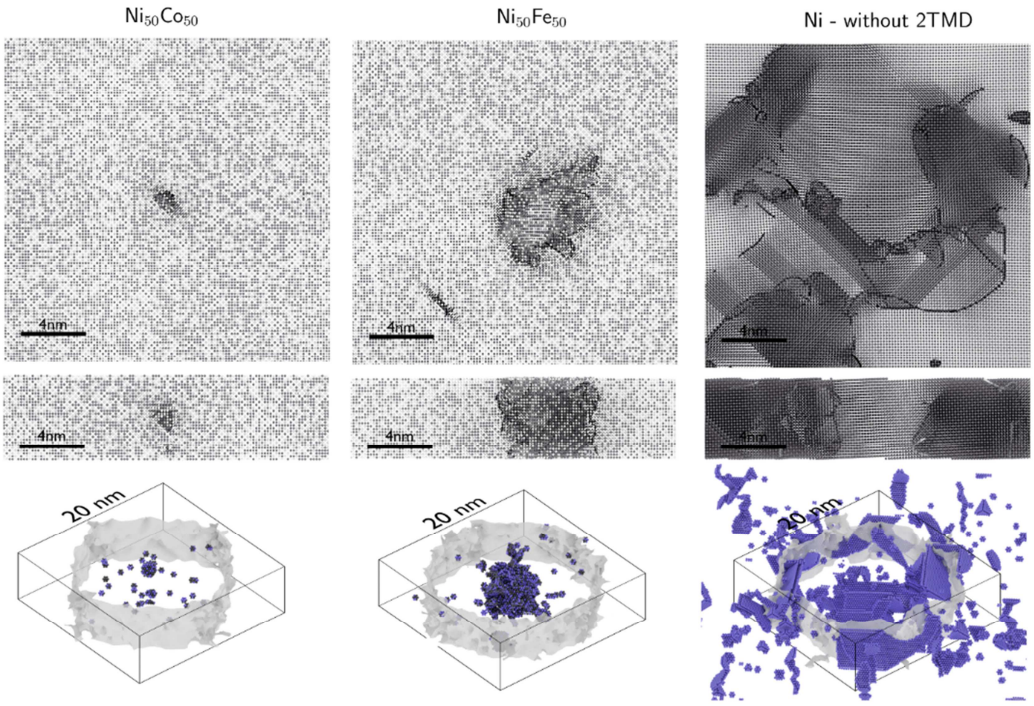

Figure 7: Residual damage. Residual damage in the simulation cells. The upmost row shows a cross section of the simulation cell cut perpendicular to the ion beam direction (c.f. figure 1) and the second row parallel. A damaged volume persists in $Ni_{50}Fe_{50}$ which is drawn as a gray surface area near the middle of the cell. In the third row, shown is the melt-solid interface when the molten radius is at its maximum and atoms with centrosymmetric parameter greater than 1. Small fragments of atoms are caused by vacancies. More detailed visualizations of the dislocations are provided in the Supplementary material. Color online only.

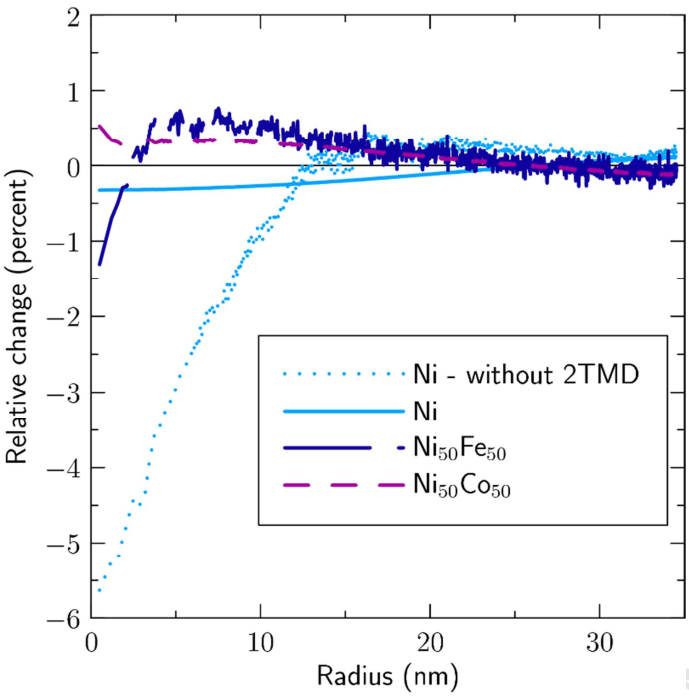

Figure 8: Title "Density plot. The residual radial density profiles after quenching and pressure relaxation. Color online only.

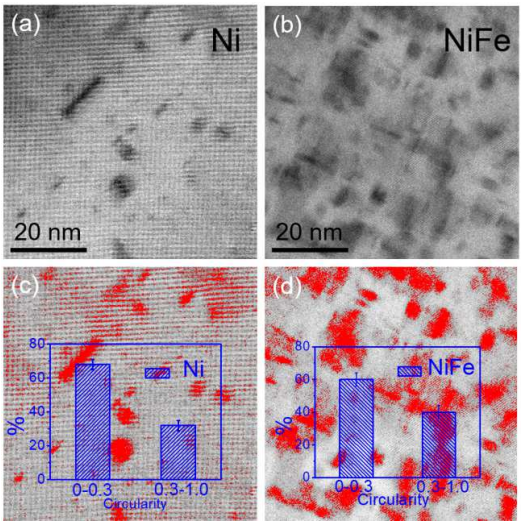

Figure 9 STEM images. Bright field (BF) STEM images of (a) Ni and (b) $Ni_{50}Fe_{50}$ irradiated using 1.542 GeV Bi to a fluence of 2×10^{12} ions cm^{-2}. The corresponding images with color thresholding in the irradiated regions are shown in (c) and (d), respectively. Red color represents defect regions with respective circularity 0.3-1 (more likely to be vacancy-type SFT) and 0-0.3 (likely to be interstitial-type dislocation loops). Color online only.

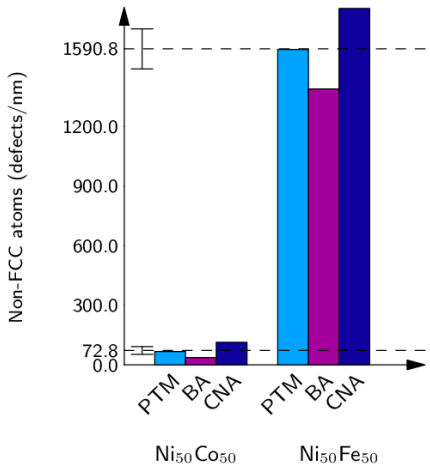

Figure 10: Number of defects. The residual defect concentrations. (PTM=Polyhedral template marching, BA=Bond angle analysis CNA=adaptive common neighbor analysis) Color online only.

Crystal	Density (g/cm^3)	Density (MD simulation, g/cm^3)	Electronic stopping power (keV/nm)	Nuclear stopping power (keV/nm)	Ion range (μm)
Ni	8.908	8.84	68.8	0.128	28.26
$Ni_{50}Co_{50}$	8.8484	8.75	66.6	0.122	28.96
$Ni_{50}Fe_{50}$	8.2326	8.28	62.8	0.113	30.49

Table 1. Target stopping powers and densities. Experimentally-determined densities and SRIM-predicted stopping powers and ion ranges for 1.542 GeV Bi ions in Ni and Ni alloys.

REFERENCES

[1] D.J. Bacon, T. Diaz de la Rubia, Molecular dynamics computer simulations of displacement cascades in metals, J. Nucl. Mater. 216 (1994) 275–290.

[2] L. Malerba, Molecular dynamics simulation of displacement cascades in α-Fe: a critical review, J. Nucl. Mater. 351 (2006) 28–38.

[3] J. Knaster, A. Moeslang, T. Muroga, Materials research for fusion, Nat. Phys. 12 (2016) 424–434.

[4] N. Itoh, D.M. Duffy, S. Khakshouri, A.M. Stoneham, Making tracks: electronic excitation roles in forming swift heavy ion tracks, J. Phys. Condens. Matter. 21 (2009) 474205.

[5] A. Iwase, S. Sasaki, T. Iwata, T. Nihira, Anomalous reduction of stage-I recovery in nickel irradiated with heavy ions in the energy range 100–120 MeV, Phys. Rev. Lett. 58 (1987) 2450–2453.

[6] H. Dammak, A. Dunlop, D. Lesueur, A. Brunelle, S. Della-Negra, Y. Le Beyec, Tracks in Metals by MeV Fullerenes, Phys. Rev. Lett. 74 (1995) 1135–1138.

[7] A. Barbu, A. Dunlop, D. Lesueur, R.S. Averback, Latent Tracks Do Exist in Metallic Materials, Europhys. Lett. 15 (1991) 37–42.

[8] G.S. Khara, S.T. Murphy, D.M. Duffy, Dislocation loop formation by swift heavy ion irradiation of metals, J. Phys. Condens. Matter. 29 (2017) 285303.

[9] F. Granberg, K. Nordlund, M.W. Ullah, K. Jin, C. Lu, H. Bei, L.M. Wang, F.

Djurabekova, W.J. Weber, Y. Zhang, Mechanism of Radiation Damage Reduction in Equiatomic Multicomponent Single Phase Alloys, Phys. Rev. Lett. 116 (2016) 135504.

[10] C. Lu, L. Niu, N. Chen, K. Jin, T. Yang, P. Xiu, Y. Zhang, F. Gao, H. Bei, S. Shi, M.-R. He, I.M. Robertson, W.J. Weber, L. Wang, Enhancing radiation tolerance by controlling defect mobility and migration pathways in multicomponent single-phase alloys, Nat. Commun. 7 (2016) 13564.

[11] Y. Zhang, G.M. Stocks, K. Jin, C. Lu, H. Bei, B.C. Sales, L. Wang, L.K. Béland, R.E. Stoller, G.D. Samolyuk, M. Caro, A. Caro, W.J. Weber, Influence of chemical disorder on energy dissipation and defect evolution in concentrated solid solution alloys, Nat. Commun. 6 (2015) 8736.

[12] E. Zarkadoula, D.M. Duffy, K. Nordlund, M.A. Seaton, I.T. Todorov, W.J. Weber, K. Trachenko, Electronic effects in high-energy radiation damage in tungsten, J. Phys. Condens. Matter. 27 (2015) 135401.

[13] A. Dunlop, D. Lesueur, A. Barbu, Evolution of microstructure resulting from high electronic excitation during swift heavy ion irradiations, J. Nucl. Mater. 205 (1993) 426–437.

[14] L. Waldecker, R. Bertoni, R. Ernstorfer, J. Vorberger, Electron-Phonon Coupling and Energy Flow in a Simple Metal beyond the Two-Temperature Approximation, Phys. Rev. X. 6 (2016) 21003.

[15] A.M. Brown, R. Sundararaman, P. Narang, W.A. Goddard, H.A. Atwater, Ab initio

phonon coupling and optical response of hot electrons in plasmonic metals, Phys. Rev. B. 94 (2016) 75120.

[16] M.I. Kaganov, I.M. Lifshitz, L. V. Tanatarov, Relaxation between electrons and the crystalline lattice, Sov. Phys. JETP. 4 (1957) 173–178.

[17] I.M. Lifshitz, M.I. Kaganov, L. V. Tanatarov, On the theory of radiation-induced changes in metals, J. Nucl. Energy. Part A. React. Sci. 12 (1960) 69–78.

[18] D.S. Ivanov, L. V Zhigilei, Combined atomistic-continuum modeling of short pulse laser melting and disintegration of metal films, Phys. Rev. B. 68 (2003) 64114.

[19] K. Nordlund, Molecular dynamics simulation of ion ranges in the 1 -- 100 keV energy range, Comput. Mater. Sci. 3 (1995) 448.

[20] A.A. Leino, S.L. Daraszewicz, O.H. Pakarinen, K. Nordlund, F. Djurabekova, Atomistic two-temperature modelling of ion track formation in silicon dioxide, EPL. 110 (2015) 16004.

[21] M.P. Allen, D.J. Tildesley, Computer Simulation of Liquids, Oxford University Press, Oxford, England, 1989.

[22] X.W. Zhou, R.A. Johnson, H.N.G. Wadley, Misfit-energy-increasing dislocations in vapor-deposited CoFe/NiFe multilayers, Phys. Rev. B. 69 (2004) 144113.

[23] J.M. Ziman, Electrons and phonons : the theory of transport phenomena in solids, Clarendon Press, 2001.

[24] P. Soven, Coherent-Potential Model of Substitutional Disordered Alloys, Phys. Rev.

156 (1967) 809–813.

[25] D.W. Taylor, Vibrational Properties of Imperfect Crystals with Large Defect Concentrations, Phys. Rev. 156 (1967) 1017–1029.

[26] G.M. Stocks, W.M. Temmerman, B.L. Gyorffy, Complete Solution of the Korringa-Kohn-Rostoker Coherent-Potential-Approximation Equations: Cu-Ni Alloys, Phys. Rev. Lett. 41 (1978) 339–343.

[27] G.D. Samolyuk, L.K. Béland, G.M. Stocks, R.E. Stoller, Electron–phonon coupling in Ni-based binary alloys with application to displacement cascade modeling, J. Phys. Condens. Matter. 28 (2016) 175501.

[28] G.S. Khara, S.T. Murphy, S.L. Daraszewicz, D.M. Duffy, The influence of the electronic specific heat on swift heavy ion irradiation simulations of silicon, J. Phys. Condens. Matter. 28 (2016) 395201.

[29] G.D. Gaspari, B.L. Gyorffy, Electron-Phonon Interactions, d Resonances, and Superconductivity in Transition Metals, Phys. Rev. Lett. 28 (1972) 801–805.

[30] A. Caro, A.A. Correa, A. Tamm, G.D. Samolyuk, G.M. Stocks, Adequacy of damped dynamics to represent the electron-phonon interaction in solids, Phys. Rev. B. 92 (2015) 144309.

[31] X.Y. Wang, D.M. Riffe, Y.-S. Lee, M.C. Downer, Time-resolved electron-temperature measurement in a highly excited gold target using femtosecond thermionic emission, Phys. Rev. B. 50 (1994) 8016–8019.

[32] W.L. McMillan, Transition Temperature of Strong-Coupled Superconductors, Phys.

Rev. 167 (1968) 331–344.

[33] Z. Lin, L. V. Zhigilei, V. Celli, Electron-phonon coupling and electron heat capacity of metals under conditions of strong electron-phonon nonequilibrium, Phys. Rev. B. 77 (2008) 75133.

[34] P.B. Allen, New method for solving Boltzmann's equation for electrons in metals, Phys. Rev. B. 17 (1978) 3725–3734.

[35] P.B. Allen, Boltzmann Theory and Resistivity of Metals, in: J.R. Chelikowsky, S.G. Louie (Eds.), Quantum Theory Real Mater., Kluwer, Boston, 1996: pp. 219–250.

[36] J. Hohlfeld, S.-S. Wellershoff, J. Güdde, U. Conrad, V. Jähnke, E. Matthias, Electron and lattice dynamics following optical excitation of metals, Chem. Phys. 251 (2000) 237–258.

[37] A.M. Chen, H.F. Xu, Y.F. Jiang, L.Z. Sui, D.J. Ding, H. Liu, M.X. Jin, Modeling of femtosecond laser damage threshold on the two-layer metal films, Appl. Surf. Sci. 257 (2010) 1678–1683.

[38] B.Y. Mueller, B. Rethfeld, Relaxation dynamics in laser-excited metals under nonequilibrium conditions, Phys. Rev. B. 87 (2013) 35139.

[39] K. Jin, B.C. Sales, G.M. Stocks, G.D. Samolyuk, M. Daene, W.J. Weber, Y. Zhang, H. Bei, Tailoring the physical properties of Ni-based single-phase equiatomic alloys by modifying the chemical complexity, Sci. Rep. 6 (2016) 20159.

[40] Y. V Petrov, K.P. Migdal, D. V Knyazev, N.A. Inogamov, P.R. Levashov, Transport properties of copper with excited electron subsystem, J. Phys. Conf. Ser. 774 (2016)

12103.

[41] S. Mazevet, M. Torrent, V. Recoules, F. Jollet, Calculations of the transport properties within the PAW formalism, High Energy Density Phys. 6 (2010) 84–88.

[42] C. Wu, L. V. Zhigilei, Microscopic mechanisms of laser spallation and ablation of metal targets from large-scale molecular dynamics simulations, Appl. Phys. A. 114 (2014) 11–32.

[43] D.S. Ivanov, Z. Lin, B. Rethfeld, G.M. O'Connor, T.J. Glynn, L. V. Zhigilei, Nanocrystalline structure of nanobump generated by localized photoexcitation of metal film, J. Appl. Phys. 107 (2010) 13519.

[44] A. Stukowski, K. Albe, Dislocation detection algorithm for atomistic simulations, Model. Simul. Mater. Sci. Eng. 18 (2010) 25016.

[45] A. Stukowski, Visualization and analysis of atomistic simulation data with OVITO–the Open Visualization Tool, Model. Simul. Mater. Sci. Eng. 18 (2009) 15012.

[46] C.L. Kelchner, S.J. Plimpton, J.C. Hamilton, Dislocation nucleation and defect structure during surface indentation, Phys. Rev. B. 58 (1998) 11085–11088.

[47] P.M. Larsen, S. Schmidt, J. Schiøtz, Robust structural identification via polyhedral template matching, Model. Simul. Mater. Sci. Eng. 24 (2016) 55007.

[48] G.J. Ackland, A.P. Jones, Applications of local crystal structure measures in experiment and simulation, Phys. Rev. B. 73 (2006) 54104.

[49] A. Stukowski, Structure identification methods for atomistic simulations of

crystalline materials, Model. Simul. Mater. Sci. Eng. 20 (2012) 45201.

[50] D.M. Duffy, N. Itoh, A.M. Rutherford, A.M. Stoneham, Making tracks in metals, J. Phys. Cond. Matter. 20 (2008) 82201.

[51] P. Kluth, C.S. Schnohr, O.H. Pakarinen, F. Djurabekova, D.J. Sprouster, R. Giulian, M.C. Ridgway, A.P. Byrne, C. Trautmann, D.J. Cookson, K. Nordlund, M. Toulemonde, Fine structure in swift heavy ion tracks in amorphous SiO2, Phys. Rev. Lett. 101 (2008) 175503.

[52] B. Afra, M.D. Rodriguez, C. Trautmann, O.H. Pakarinen, F. Djurabekova, K. Nordlund, T. Bierschenk, R. Giulian, M.C. Ridgway, G. Rizza, N. Kirby, M. Toulemonde, P. Kluth, SAXS investigations of the morphology of swift heavy ion tracks in α-quartz, J. Phys. Condens. Matter. 25 (2013) 45006.

[53] Y. Zhang, S. Zhao, W.J. Weber, K. Nordlund, F. Granberg, F. Djurabekova, Atomic-level heterogeneity and defect dynamics in concentrated solid-solution alloys, Curr. Opin. Solid State Mater. Sci. 21 (2017) 221–237.

[54] Z.G. Wang, C. Dufour, E. Paumier, M. Toulemonde, The S e sensitivity of metals under swift-heavy-ion irradiation: a transient thermal process, J. Phys. Condens. Matter. 6 (1994) 6733–6750.

GRAPHICAL ABSTRACT